Clays Clay Miner.
https://doi.org/10.1007/s42860-021-00168-z

The Composition and Growth Mechanism of Coexisting $4M_2$ and $4A_8$ Biotite Polytypes from Rhyolite of Long Valley Caldera, California

Jiaxin Xi · Yiping Yang · Lingya Ma · Hongping He · Huifang Xu · Jianxi Zhu · Jingming Wei

Accepted: 11 December 2021

Abstract Polytypism is common in micas, and the frequency of polytype occurrence is believed to be related closely to the crystallization conditions and chemical compositions of the corresponding fluids and melts. Coexisting multiple standard and complex/disordered polytypes in igneous rocks generally reflect a complicated magma evolution history. The purpose of the current study was to clarify the origin of coexisting biotite polytypes and their growth mechanism. Micro-X-ray diffraction (μXRD) and transmission electron microscopy (TEM) were used to investigate Fe-rich biotite phenocrysts in rhyolite from the Long Valley Caldera, California, USA. The μXRD analyses characterized various polytypes, and TEM observations revealed that common polytypes (e.g. 1*M*, $2M_1$, and 3*T*) and rare polytypes (e.g. $4M_2$ and $4A_8$) coexist within biotite monocrystals. The two 4-layer polytypes of Fe-rich biotite, $4M_2$ and $4A_8$, were identified via selected-area electron diffraction (SAED) and high-resolution scanning transmission electron microscopy (HRSTEM) at the atomic resolution, with unique stacking sequences ([0222] for $4M_2$ and $[00\bar{2}\bar{2}]$ for $4A_8$). Energy-dispersive X-ray spectroscopy (EDS) results showed differences in their chemical compositions, especially Fe and K. The $4A_8$ polytype is reported for the first time. The present study suggested that environmental changes, such as rapid cooling and inhomogeneous compositional distribution, led to chemical and structural oscillations and complex nucleation of the two 4-layer polytypes. Screw dislocations producing spiral growth enhance polytype stability and form ordered long-period/complex polytypes. These results are useful to understand the origin of long-period/complex polytypes and the intergrowths of diverse polytypes formed in non-equilibrium crystallization environments.

Keywords Biotite Non-equilibrium crystallization · Polytype · Rhyolite · Screw dislocation · STEM

Supplementary Information The online version contains supplementary material available at https://doi.org/10.1007/s42860-021-00168-z.

J. Xi · Y. Yang · L. Ma (✉) · H. He · J. Zhu · J. Wei
CAS Key Laboratory of Mineralogy and Metallogeny/ Guangdong Provincial Key Laboratory of Mineral Physics and Materials, Guangzhou Institute of Geochemistry, Chinese Academy of Sciences, Guangzhou 510640, China
e-mail: malingya@gig.ac.cn

J. Xi · Y. Yang · L. Ma · H. He · J. Zhu · J. Wei
CAS Center for Excellence in Deep Earth Science, Guangzhou 510640, China

J. Xi · L. Ma · H. He · J. Zhu · J. Wei
University of Chinese Academy of Sciences, Beijing 100049, China

H. Xu
Department of Geoscience, University of Wisconsin-Madison, 1215 West Dayton Street, Madison, WI 53706, USA

Published online: 08 February 2022

Introduction

Micas are major rock-forming minerals that are abundant in the Earth's continental crust (Brigatti & Guggenheim, 2002). They are regarded as recorders of the evolution of metallogenic environments and of changes in ore-forming fluid conditions (Lacalamita et al., 2012a; Xu & Veblen, 1995). Micas are 2:1 phyllosilicates (or T-O-T type layer silicates), with monovalent and, less frequently, divalent cations occurring in the interlayer regions (Nespolo, 1999; Pauling, 1930). An ideal single mica layer is characterized by monoclinic $C2/m$ space group symmetry, the surface oxygen atoms of the tetrahedral sheets in a mica layer are related by a sixfold axis perpendicular to the (001) plane (Bailey, 1984; Nespolo & Ďurovič, 2002; Ross et al., 1966). Therefore, a single layer can fit laterally on an adjacent layer in six possible orientations, with relative layer rotations of $0°, \pm 60°, \pm 120°$, and 180° about an axis (c^*) perpendicular to (001) (Bailey, 1984; Ferraris & Ivaldi, 2002; Ross et al., 1966). Mica polytypism is thus determined by the number of layers that can be arranged in a particular rotational sequence. A graphical method describing the $1M$, $2M_1$, $2M_2$, $2O$, $3T$, and $6H$ polytypes was presented for stacking sequences of the six standard mica polytypes (Guinier et al., 1984; Ross et al., 1966; Smith & Yoder, 1956). In addition, Ross et al. (1966) derived all 4-layer polytypes, and Xu and Veblen (1995) derived all 5-layer polytypes involving 120° rotations.

Mica polytypism has been well investigated for a wide range of geological settings, and the frequency of occurrence of mica polytypes has been shown to be a function of crystallization environments (Bailey, 1984; Fregola et al., 2009; Lacalamita et al., 2012b; Ross et al., 1966; Smith & Yoder, 1956; Xu & Veblen, 1995). For example, the $1M$ polytype is the most common in biotite, followed by $2M_1$ and $3T$, and they may coexist with other long-period/complex polytypes (Baronnet & Kang, 1989; Bozhilov et al., 2009; Fregola et al., 2009; Nespolo, 1999, 2001; Pignatelli et al., 2011; Ross et al., 1966). An unusual arrangement of atoms or staggering deviation of layers leads to a change in the local symmetry (Baronnet & Kang, 1989; Nespolo & Ďurovič, 2002). Biotite with long-period/complex polytypes occurs frequently in volcanic rocks due to non-equilibrium and a complex crystallization history (Fregola & Scandale, 2011; Ross et al., 1966; Sunagawa et al., 1968; Tomisaka, 1958, 1962; Vand & Hanoka, 1967; Xu & Veblen, 1995). Thus far, complex biotite polytypes have been identified in nature, such as several 4-layer polytypes (Pignatelli et al., 2011; Ross et al., 1966; Takeda & Donnay, 1965; Zhukhlistov et al., 1988), 5-layer polytypes (Baronnet, 1992; Pignatelli & Nespolo, 2011; Xu & Veblen, 1995), 32- and 36-layer mixed rotation polytypes (Kogure & Nespolo, 1999), and a long-periodicity 94-layer polytype (Fregola & Scandale, 2011). The coexistence of short- and long-period polytypes in the same occurrence is, however, extremely rare (Pignatelli et al., 2016; Ross et al., 1966), and the origin of this coexistence is poorly understood.

Several hypotheses have been proposed to explain the formation of polytypes and polytype coexistence (Baronnet & Kang, 1989; Fregola & Scandale, 2011; and references therein), in which the effect of chemical composition rather than structure considerations is one of the most controversial. Some studies proposed that the chemical composition is an important controlling factor (Baronnet & Kang, 1989; Baronnet et al., 1993; Fregola et al., 2009; Güven & Burnham, 1967; Stöckhert, 1985; Xu & Veblen, 1995). However, different polytypes with similar compositions have been found to coexist (Bigi & Brigatti, 1994; Brigatti et al., 2008; Fregola & Scandale, 2011; Lacalamita et al., 2012a; Laurora et al., 2007; Takeda & Ross, 1975). The formation of mica polytypes is believed to be a two-stage process involving nucleation and crystal growth (Baronnet & Kang, 1989). During a rapid crystallization of biotite in extrusive rocks, the rapid change in physicochemical conditions induces complex structural oscillations (Xu & Veblen, 1995), leading to nucleation at non-equilibrium conditions (Pignatelli et al., 2016; Ross et al., 1966). Although theories involving screw dislocation and mica polytypes seem to rationalize the occurrence of long-period complexes (Baronnet & Kang, 1989; Pignatelli et al., 2011; Ramsdell, 1947; Sunagawa et al., 1968; Tomisaka, 1958, 1962), such theories are still under debate (Fregola & Scandale, 2011; and references therein) because of a lack of direct evidence at the atomic scale.

High-resolution transmission electron microscopy (HRTEM) is a powerful technique to reveal the stacking sequence of micas (Fregola & Scandale, 2011; Nespolo & Ďurovič, 2002; Xu & Veblen,

1995). The stacking sequences of long-period and inhomogeneous mica polytypes require HRTEM images along two zone axes rotated 30° apart about the *c*-axis (e.g. [010] and [110] zone axes). The objective of the current study was to use HRTEM in combination with other in situ microscopy techniques to investigate and identify the coexisting polytypes of the biotite in rhyolite from the Long Valley Caldera, California, USA. This is to be followed by a discussion of a possible formation mechanism related to non-equilibrium nucleation and spiral growth in order to understand the rare coexistence of standard and complex polytypes of biotite. The work aimed to provide new evidence and insight to explain the structure and genesis of complex polytypes of biotite and their coexistence with other polytypes.

Materials and Methods

Biotite phenocrysts occurring as fine platelets without alteration were collected from a rhyolite at the Long Valley Caldera. The Long Valley magmatic system occurs along the eastern part of the Sierra Nevada Mountains on the western edge of the Basin and Range Province (Metz & Mahood, 1991). The caldera remains thermally active, with numerous hot springs and fumaroles, and the rocks have undergone considerable deformation, seismicity, and other disturbances in recent years. A major explosive eruption occurred at 0.73 Ma, leaving behind in the caldera a basalt containing a large volume of pre-caldera high-silica rhyolite lava; biotite occurs as the most abundant mafic phenocryst in the lavas. Ash-fall deposits containing biotite also occur (Metz & Mahood, 1991).

Single biotite platelets were examined via light microscopy. For the micro-X-ray diffraction (μXRD) analysis, patterns were recorded using a Rigaku D-MAX RAPID-V diffractometer (Tokyo, Japan) with a microfocus rotating anode source (MicroMax-007HFM X-ray generator of Rigaku; Tokyo, Japan) and a curved imaging plate detector. The diffractometer was operated with CuKα radiation (λ = 1.5418 Å) generated at 40 kV and 30 mA. The μXRD patterns were collected in reflection mode using a 0.03 mm collimator and a collection time of 1000 s. The data were collected as two-dimensional images and then converted into º2θ-intensity profiles using the Rigaku *2DP* software. For each XRD pattern the interpretable º2θ region was selected manually.

The elemental composition of biotite was determined on a JEOL JXA-8230 (Tokyo, Japan) electron probe microanalyzer (EPMA) at operating conditions of 15 kV, 20 nA, and ~3 μm beam diameter. The ZAF correction method was used for data reduction. The standards used for data correction were orthoclase for K, albite for Na, BaF_2 for F, chrome-diopside for Si and Ca, olivine for Mg, magnetite for Fe, rutile for Ti, rhodonite for Mn, and pure aluminum metal for Al. All the mentioned standard metals/minerals for EPMA were produced by Structure Probe, Inc (SPI) Supplies (West Chester, Pennsylvania, USA). Because of a relatively large Fe content, the biotite samples were identified to be Fe-rich (Guggenheim et al., 2002).

Biotite samples were oriented and embedded in epoxy resin and dried at 100°C for 5 h. After solidification and cooling, ultrathin sections ~70 nm thick were sliced with a diamond knife using a Leica EM UC7 ultramicrotome (Wetzlar, Germany). The ultrathin samples were then arranged on carbon-coated copper microgrids, as described by He et al. (2021). The TEM and related investigations were performed at 200 kV voltage using an FEI Talos F200S field-emission transmission electron microscope (Brno, Czech Republic), coupled with two SuperX high-resolution energy-dispersive spectrometers (Thermo Fisher, Brno, Czech Republic) and a high-angle annular dark-field (HAADF) detector. Z-contrast images were acquired using a camera length of 160 mm to maximize the contrast variations between different atoms in the HAADF images (Xu et al., 2014, 2015). High-resolution scanning transmission electron microscopy (HRSTEM) images were filtered using *Gatan Digital Micrograph* (version 3.11; AMETEK, Inc., San Diego, California, USA) to remove the noisy contrast generated by amorphous materials.

The energy-dispersive X-ray spectroscopy (EDS) information from the investigated samples was collected from thin areas under the same conditions to ensure consistency of intensity and accurate comparison to the standards. The EDS sampling time was 6 min to prevent any beam damage to the biotite sample; the spot size was ~1 nm, the scanning range was ~100 nm × 300 nm, the sample thickness

was < 30 nm, and the stage tilt was zero. The EDS semi-quantitative analytical lines were NaKα, MgKα, AlKα, SiKα, KKα, TiKα, MnKα, and FeKα (Figs. S4a,b). The mass concentrations of cation oxides (e.g. SiO_2, MgO) were calculated from the element ratio and *k*-factors. The composition of a standard biotite (calibrated using the electron probe microanalyzer) was used to quantify the elemental fractions of Al, Mg, Fe, Ti, Mn, K, and Na in the samples (Table S1).

Results

Micro-XRD and SAED Patterns

Polytypes of Fe-rich biotite can be determined by the characteristic reflections in X-ray diffraction patterns (Takeda & Ross, 1975). The micro X-ray diffraction (μXRD) patterns (Figs. 1a and S1a,b) show coexisting 1*M* and $2M_1$ polytypes and $2M_1$ and 3*T* polytypes, respectively. The reflections at 34.04°2θ (2.63 Å), 27.52°2θ (3.24 Å), and 54.53°2θ (1.68 Å) in the top μXRD pattern were attributed to the $\bar{1}31$, 112, and $\bar{1}35$ reflections of the 1*M* Fe-rich biotite, respectively (PDF card No. 80–1108 CuKα). In the lower μXRD pattern, the diffraction peaks at 26.25°2θ (3.39 Å), 30.62°2θ (2.91 Å), 33.11°2θ (2.70 Å), and 35.84°2θ (2.50 Å) were attributed to the 106, 108, 109, and $\bar{1}14$ reflections of the 3*T* Fe-rich biotite (PDF card No.73–1659 CuKα), respectively. Note that the reflections at 27.28°2θ (3.28 Å), 36.83°2θ (2.44 Å), and 55.09°2θ (1.67 Å) in the two μXRD patterns correspond to the 114, 133, and 139 reflections of the $2M_1$ Fe-rich biotite (PDF card No.83–1366 CuKα), respectively. The 1*M*, $2M_1$, and 3*T* polytypes were identified also by SAED patterns recorded from the [110] zone axis (Fig. 1b–d). The μXRD and SAED patterns (Fig. 1) revealed the polytype mixture in the Fe-rich biotite monocrystal, indicating that a complex polytype occurs in the Fe-rich biotite from the rhyolite.

[010] Zone Axis SAED Pattern and HRTEM Image

The SAED patterns of 1*M*, $2M_1$, 3*T,* and the two 4-layer period polytypes taken along the [010] zone axis were identical (Fig. 1e), and the polytypes cannot be distinguished from each other. The representative SAED pattern showed that the *h*0*l* reflections fit the characteristics of the subfamily-A biotite (Nespolo, 1999). In addition, as shown in the HRTEM image from the [010] zone axis (Fig. 1f), the projection of the stacking vectors points to the right, producing a shift of *a*/6 along the *a* direction, which agrees well with the SAED patterns along the [010] direction (Nespolo, 1999). Considering the space-fixed azimuthal orientation symbols of Zvyagin (as labels shown in lower right of Fig. 1f), each stagger of these stacking vectors characterized by a 120° rotation between the adjacent layers produced a vector parallel to the [100] direction and equal to + *a*/6 for both the stacking vectors 2 and 4 pointing to the right. For stacking vector 6, the stagger could be –*a*/3 pointing to the left, which is equivalent to + *a*/6 pointing to the right, when viewed along the [010] zone axis (Fregola & Scandale, 2011; Zvyagin, 1987, 1997). The HRTEM images from the [010] zone axis suggest the occurrence of subfamily-A of mica polytypes in the samples, but the stacking vectors 2, 4, and 6 cannot be discriminated. To obtain the "Ross-Takeda-Wones (RTW)" expression for distinguishing and describing mica polytypes (Ross et al., 1966), layer rotations associated with image shifts need to be determined. HRTEM images viewed along the [110] or [$1\bar{1}0$] zone axes provide important information about stacking orientation for the polytypes involving 120° rotations only (Banfield & Murakami, 1998; Baronnet & Kang, 1989; Fregola & Scandale, 2011; Kogure, 2002; Kogure & Banfield, 1998; Xu & Veblen, 1995).

[110] Zone-axis of the two 4-layer Period Polytypes

The SAED patterns along the [110] zone axis (Fig. 2a, b) showed strong diffraction spots in both 00 *l* and 1 $1\bar{1}$ rows, with a repetition of ~ 1/10 $Å^{-1}$, and three additional diffraction spots belonging to the 4-layer polytype that occurred between the host strong spots in the 1 $1\bar{1}$ row. The diffraction spot intensities of the two SAED patterns were significantly different (Fig. 2a, b). The diffraction spots in Fig. 2a showed intensity characteristics: strong–weak–weak–weak–strong … (Fig. 2c), corresponding to the [0222] stacking sequences. The diffraction spots in Fig. 2b exhibited intensity distribution: very strong–strong–very weak–weak–very

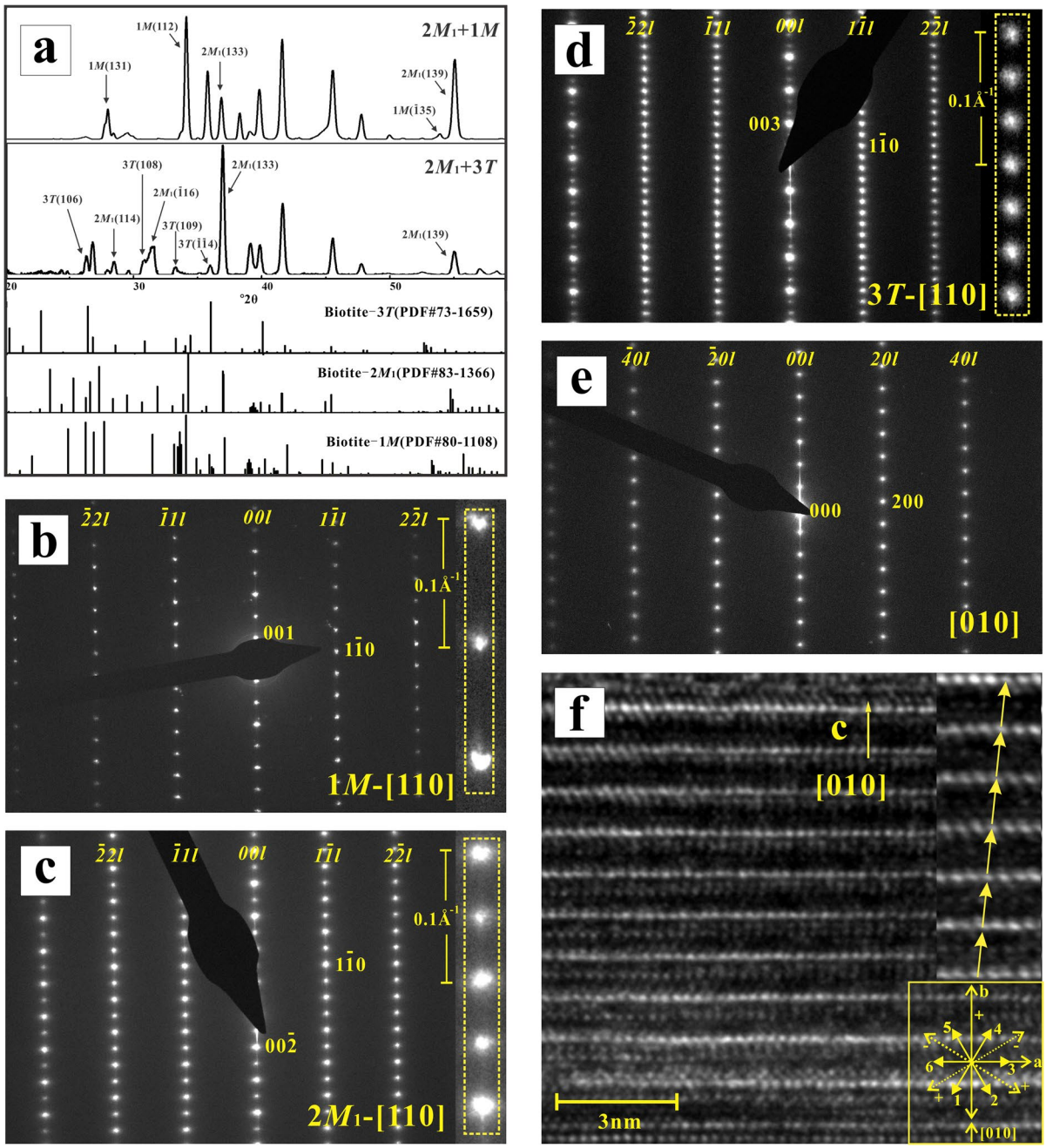

Fig. 1 μ-XRD patterns, SAED patterns, and HRTEM image of biotite crystals: **a** Representative μ-XRD patterns of biotite samples and standard 1*M,* $2M_1$, and 3*T*-polytype PDF cards. **b,d** SAED patterns of **b** 1*M*, **c** $2M_1$, and **d** 3*T* biotite crystals. **e**,**f** Representative HRTEM image **e** and SAED pattern **f** from [010] zone axis. Arrows in **f** are the projection of the stacking vectors. The space-fixed azimuthal orientation symbols of Zvyagin in (001) projection is labeled at the lower right, with the length of all stacking vectors being equal to *a*/3. As the orientation symbols show, when viewed along [010], both stacking vectors 2 and 4 can produce component vectors that are parallel to the [100] direction (*a*-axis direction) and is equal to + *a*/6

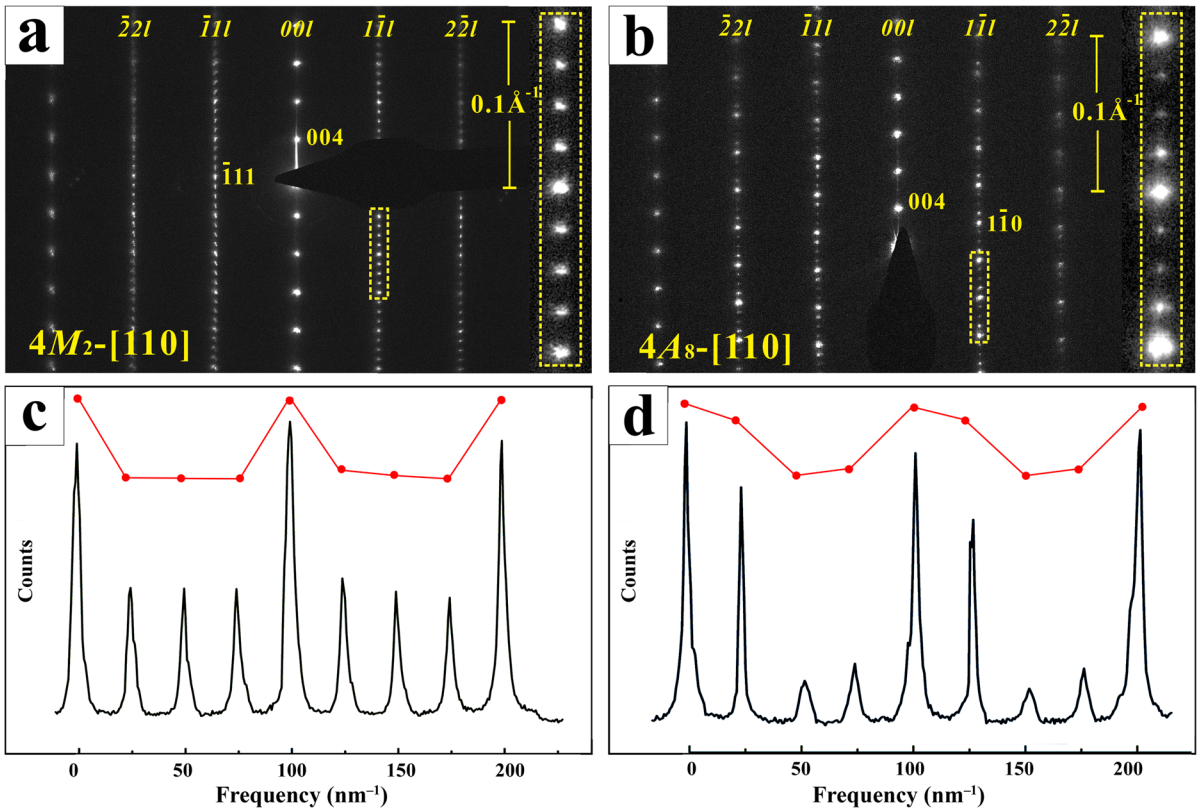

Fig. 2 SAED patterns of the two 4-layer polytypes: SAED patterns of **a** $4M_2$ biotite crystal and **b** $4A_8$ biotite crystal. **c**,**d** Intensity counts of the two repetition periods of *hkl* reflections, indicated by the yellow dotted boxes in **a** and **b**. Red spots and line segments indicate the trend of the intensity changes

strong … (Fig. 2d), attributed to the [00$2\bar{2}$] stacking sequences. Observations and calculations suggested that the intensity distribution of reflections in the reciprocal lattice rows parallel to the c^*-axis can be used to infer the stacking sequences corresponding to mica polytypes (Ross et al., 1966; Takeda & Ross, 1975, 1995). Two 4-layer polytypes that were theoretically speculated by Ross et al. (1966) were identified as $4M_2$ (Fig. 2a) and $4A_8$ (Fig. 2b), and the latter is the first report in natural samples.

The low-magnification TEM image captured along the [110] zone axis of the 4-layer-polytype Fe-rich biotite domain did not show sufficient variations in contrast, and polytype characteristics could not be determined (Fig. S2a). One-dimensional (1D) lattice fringe images were useful for identifying polytypes (Fregola & Scandale, 2011; Iijima & Buseck, 1978). The TEM image of a tilted Fe-rich biotite specimen (Fig. S2a), rotated ~3° about the [110] direction, showed clear variations in contrast (Fig. S2b). Along the *c*-axis, distinctions containing four mica layers repeated periodically more than 15 times. The 1D TEM images of Fe-rich biotite monocrystals displayed dozens of four-layer polytype domains, and two representative biotite domains containing $4M_2$ and $4A_8$ polytypes are shown in Fig. 3a, b. The low-magnification 1D TEM images showed regular 4-layer (4 nm) periodicity in the range of hundreds of nanometers (Figs. 3a, b and S3a,b, with enlargements of the yellow dashed squares). The fast Fourier transform (FFT) patterns showed that the repetitive period of both $4M_2$ and $4A_8$ are similar but the sub-cell spot intensities are different for each polytype (Figs. 3a, b and S3a,b, inset at the bottom right), corresponding to different stacking sequences.

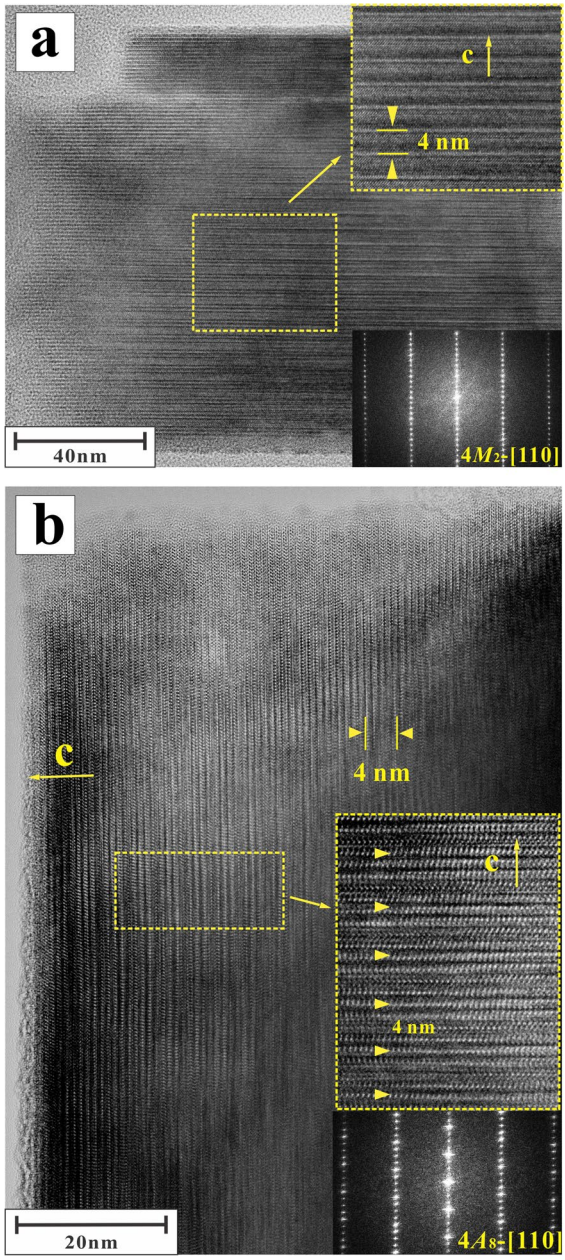

Fig. 3 One-dimensional (1D) HRTEM images of representative four-layer biotite domains, with fast Fourier transform (FFT) patterns (bottom right of each image) showing a periodic shift after every four layers. **a** 1D image of the $4M_2$ biotite domain with the enlarged HRTEM image in the yellow rectangle, and FFT pattern. **b** 1D image of the $4A_8$ biotite domain with enlarged HRTEM image in the yellow rectangle, and FFT pattern

The stacking sequences of the two 4-layer polytype domains were determined via the atomic-resolution HAADF–STEM images taken along the [110] zone axis (Fig. 4a, b). In the HAADF–STEM (or Z-contrast) images, the intensity (I) of the atom spots is proportional to the atomic number (Z) and the number of atoms (m) along the beam direction (i.e. $I \sim mZ^n$) (Pennycook, 2002). The HAADF-STEM images (Fig. 4a, b) show that the brighter rows were the octahedral sheets (O columns) in the T-O-T sandwiched unit layer, because of the existence of metal cations (i.e. Fe^{2+}) with relatively large atomic numbers. Owing to the resolution limit of the measurement instrument, the cations in the O columns could not be distinguished as separated spots. The darker spots adjacent to the O columns represented tetrahedral sheets (T columns), whereas the interlayer K columns are between two T-O-T unit layers, with a distance of ~0.45 nm between the two adjacent K cations when viewed from the [110] zone axis (Fig. 4a, b). The stacking sequences of 4-layer polytypes (Fig. 4a, b) are [0222] and [002$\bar{2}$], which were determined by simulation as $4M_2$ and $4Tc_8$ (i.e. $4A_8$), respectively, in Ross et al. (1966). The $4M_2$ polytype with a stacking sequence of [0222] meant that these Fe-rich biotite domains had monoclinic ($C2$) symmetry based on $3T$ ($P3_112$ or $P3_212$) and $1M$, with a preserved two-fold axis. On the other hand, the $4A_8$ polytype had a stacking sequence of [002$\bar{2}$] with a monoclinic ($C\bar{1}$) symmetry, as a result of the preservation of $\bar{1}$ (e.g. the inversion center) from the packing of $2M_1$ and $1M$ (off by 60°) only. Both $2M_1$ and $1M$ have unit-cell parameters of $a = 0.53$ nm, $b = 0.92$ nm, and $c = 4.00$ nm, where $\beta = 95.1°$.

Composition Analysis

Each Fe-rich biotite domain was analyzed using EDS (see Materials and Methods). The average electron probe microanalysis (EPMA) result was used as the standard mica composition to obtain the k-factors of each element (Table S1). The formulae calculated using the chemical compositions of several $4M_2$ and $4A_8$ Fe-rich biotite domains, corrected by k-factors, are listed in Table 1. The elemental distribution in a domain was generally homogeneous for a specific polytype (Table 1) but slightly different for other polytypes (Table 1, Figs. 5a and S4-5). The average structural formulae of the two 4-layer Fe-rich biotite polytypes were calculated based on 11 oxygen atoms as follows:

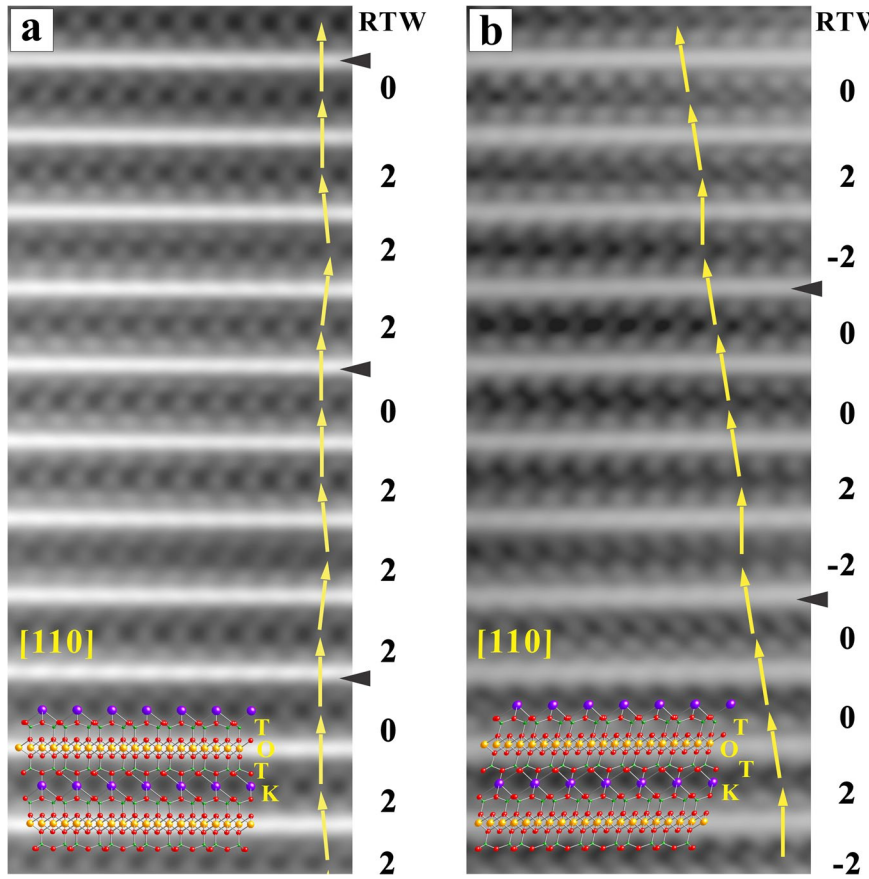

Fig. 4 High-resolution, high-angle annular dark-field scanning transmission electron microscopy images of the two 4-layer long-period biotite domains ($4M_2$ and $4A_8$). The stacking sequences with the RTW symbols are **a** [0222] and **b** [002 $\bar{2}$]. The ball-and-stick model displays the corresponding structures of biotite along the [110] zone axis. The purple, green, red, and yellow spheres represent K, (Si, Al), O, and (Mg, Fe), respectively

EPMA:

$$(K_{0.89}Na_{0.08})_{\Sigma=0.97}(Ti_{0.27}Mn_{0.03}Fe_{1.61}Mg_{0.95})$$
$$\Sigma=2.86(Si_{2.84}Al_{1.16})_{\Sigma=4.00}O_{10}(F_{0.08}Cl_{0.02}OH_{1.90})_{\Sigma=2.00}.$$

EDS:

$$4M_2 - (K_{0.91}Na_{0.08})_{\Sigma=0.99}(Mg_{0.93}Fe_{1.66}Mn_{0.03}Ti_{0.27})$$
$$\Sigma=2.89(Si_{2.84}Al_{1.16})_{\Sigma=4.00}O_{10}(OH)_2,$$
$$4A_8 - (K_{0.86}Na_{0.08})_{\Sigma=0.94}(Mg_{0.97}Fe_{1.58}Mn_{0.03}Ti_{0.27})$$
$$\Sigma=2.84(Si_{2.85}Al_{1.15})_{\Sigma=4.00}O_{10}(OH)_2.$$

In this calculation, the Fe was assumed to exist as Fe^{2+}, which is the dominant valence state of Fe ions in the samples (Metz & Mahood, 1991), and share the octahedral sites with Mg ions. The estimated standard deviations (ESD) of Fe, K, Si, and Mg were calculated based on compositional data from EPMA (Table S2), with the formula (Hooper & Eloranta, 1986):

$$\mathrm{ESD(z)} = \left\{ \frac{1}{N} \sum_{i=1}^{N} \left[P(z) i z^2 - \overline{P(z) z^2} \right]^2 \right\}^{1/2} \quad (1)$$

where N, z, and P are the number of compositional data, the element type, and specific content value (stoichiometry used here), respectively. After correction, the EDS calculation results, on average, agreed well with the EPMA test results. The ESD of elements calculated and reported in Table S2 showed that all estimated standard deviations were <5.70%. The effect of thickness and local inhomogeneity had been eliminated as much as possible. A comparison

Table 1 Biotite formulae of $1M$-, $4A_8$-, and $4M_2$- biotite based on EDS ratios

Polytype	SpotNo	Formulae
$1M$	1	$(K_{0.92}Na_{0.08})_{\sum=1.00}(Mg_{0.92}Fe_{1.61}Mn_{0.03}Ti_{0.28})_{\sum=2.84}(Si_{2.87}Al_{1.13})_{\sum=4.00}O_{10}(OH)_2$
	2	$(K_{0.92}Na_{0.08})_{\sum=1.00}(Mg_{0.93}Fe_{1.64}Mn_{0.03}Ti_{0.27})_{\sum=2.87}(Si_{2.86}Al_{1.14})_{\sum=4.00}O_{10}(OH)_2$
	3	$(K_{0.91}Na_{0.08})_{\sum=1.00}(Mg_{0.91}Fe_{1.64}Mn_{0.03}Ti_{0.27})_{\sum=2.85}(Si_{2.88}Al_{1.12})_{\sum=4.00}O_{10}(OH)_2$
	4	$(K_{0.92}Na_{0.08})_{\sum=1.00}(Mg_{0.94}Fe_{1.63}Mn_{0.03}Ti_{0.27})_{\sum=2.87}(Si_{2.86}Al_{1.14})_{\sum=4.00}O_{10}(OH)_2$
	5	$(K_{0.90}Na_{0.08})_{\sum=0.98}(Mg_{0.95}Fe_{1.69}Mn_{0.04}Ti_{0.26})_{\sum=2.93}(Si_{2.75}Al_{1.25})_{\sum=4.00}O_{10}(OH)_2$
	6	$(K_{0.91}Na_{0.08})_{\sum=1.00}(Mg_{0.91}Fe_{1.64}Mn_{0.03}Ti_{0.27})_{\sum=2.85}(Si_{2.88}Al_{1.12})_{\sum=4.00}O_{10}(OH)_2$
	7	$(K_{0.91}Na_{0.08})_{\sum=0.99}(Mg_{0.93}Fe_{1.71}Mn_{0.03}Ti_{0.27})_{\sum=2.94}(Si_{2.83}A_{1.17})_{\sum=4.00}O_{10}(OH)_2$
	Avg	$(K_{0.91}Na_{0.08})_{\sum=0.99}(Mg_{0.93}Fe_{1.66}Mn_{0.03}Ti_{0.27})_{\sum=2.89}(Si_{2.84}Al_{1.16})_{\sum=4.00}O_{10}(OH)_2$
$4A_8$	1	$(K_{0.81}Na_{0.07})_{\sum=0.88}(Mg_{0.92}Fe_{1.52}Mn_{0.04}Ti_{0.31})_{\sum=2.79}(Si_{2.86}Al_{1.14})_{\sum=4.00}O_{10}(OH)_2$
	2	$(K_{0.90}Na_{0.08})_{\sum=0.97}(Mg_{0.93}Fe_{1.62}Mn_{0.03}Ti_{0.28})_{\sum=2.86}(Si_{2.80}Al_{1.20})_{\sum=4.00}O_{10}(OH)_2$
	3	$(K_{0.80}Na_{0.08})_{\sum=0.88}(Mg_{0.92}Fe_{1.57}Mn_{0.04}Ti_{0.30})_{\sum=2.82}(Si_{2.84}Al_{1.16})_{\sum=4.00}O_{10}(OH)_2$
	4	$(K_{0.81}Na_{0.09})_{\sum=0.90}(Mg_{0.98}Fe_{1.63}Mn_{0.03}Ti_{0.25})_{\sum=2.90}(Si_{2.75}Al_{1.25})_{\sum=4.00}O_{10}(OH)_2$
	5	$(K_{0.84}Na_{0.08})_{\sum=0.93}(Mg_{0.98}Fe_{1.59}Mn_{0.02}Ti_{0.26})_{\sum=2.85}(Si_{2.86}Al_{1.14})_{\sum=4.00}O_{10}(OH)_2$
	6	$(K_{0.86}Na_{0.08})_{\sum=0.93}(Mg_{0.99}Fe_{1.59}Mn_{0.03}Ti_{0.27})_{\sum=2.89}(Si_{2.85}Al_{1.15})_{\sum=4.00}O_{10}(OH)_2$
	7	$(K_{0.89}Na_{0.08})_{\sum=0.97}(Mg_{0.97}Fe_{1.53}Mn_{0.03}Ti_{0.27})_{\sum=2.80}(Si_{2.88}Al_{1.12})_{\sum=4.00}O_{10}(OH)_2$
	8	$(K_{0.91}Na_{0.08})_{\sum=0.98}(Mg_{0.97}Fe_{1.56}Mn_{0.02}Ti_{0.23}Al_{0.05})_{\sum=2.83}(Si_{2.89}Al_{1.11})_{\sum=4.00}O_{10}(OH)_2$
	9	$(K_{0.90}Na_{0.08})_{\sum=0.98}(Mg_{1.00}Fe_{1.55}Mn_{0.01}Ti_{0.23}Al_{0.04})_{\sum=2.84}(Si_{2.87}Al_{1.13})_{\sum=4.00}O_{10}(OH)_2$
	10	$(K_{0.86}Na_{0.08})_{\sum=0.93}(Mg_{0.99}Fe_{1.59}Mn_{0.03}Ti_{0.27})_{\sum=2.89}(Si_{2.85}Al_{1.15})_{\sum=4.00}O_{10}(OH)_2$
	11	$(K_{0.89}Na_{0.08})_{\sum=0.97}(Mg_{0.97}Fe_{1.53}Mn_{0.03}Ti_{0.27})_{\sum=2.80}(Si_{2.88}Al_{1.12})_{\sum=4.00}O_{10}(OH)_2$
	12	$(K_{0.84}Na_{0.08})_{\sum=0.93}(Mg_{0.98}Fe_{1.59}Mn_{0.02}Ti_{0.26})_{\sum=2.85}(Si_{2.86}Al_{1.14})_{\sum=4.00}O_{10}(OH)_2$
	Avg	$(K_{0.86}Na_{0.08})_{\sum=0.94}(Mg_{0.97}Fe_{1.58}Mn_{0.03}Ti_{0.27})_{\sum=2.84}(Si_{2.85}Al_{1.15})_{\sum=4.00}O_{10}(OH)_2$
$4M_2$	1	$(K_{0.87}Na_{0.12})_{\sum=0.98}(Mg_{0.89}Fe_{1.64}Mn_{0.03}Ti_{0.27})_{\sum=2.83}(Si_{2.90}Al_{1.10})_{\sum=4.00}O_{10}(OH)_2$
	2	$(K_{0.89}Na_{0.09})_{\sum=0.98}(Mg_{0.99}Fe_{1.65}Mn_{0.03}Ti_{0.25})_{\sum=2.91}(Si_{2.76}Al_{1.24})_{\sum=4.00}O_{10}(OH)_2$
	3	$(K_{0.95}Na_{0.04})_{\sum=1.00}(Mg_{0.97}Fe_{1.72}Mn_{0.03}Ti_{0.28})_{\sum=3.00}(Si_{2.76}Al_{1.24})_{\sum=4.00}O_{10}(OH)_2$
	4	$(K_{0.91}Na_{0.09})_{\sum=0.99}(Mg_{0.93}Fe_{1.63}Mn_{0.03}Ti_{0.27})_{\sum=2.86}(Si_{2.86}Al_{1.14})_{\sum=4.00}O_{10}(OH)_2$
	5	$(K_{0.93}Na_{0.07})_{\sum=1.00}(Mg_{0.94}Fe_{1.67}Mn_{0.03}Ti_{0.26})_{\sum=2.90}(Si_{2.85}Al_{1.15})_{\sum=4.00}O_{10}(OH)_2$
	6	$(K_{0.92}Na_{0.08})_{\sum=1.00}(Mg_{0.92}Fe_{1.61}Mn_{0.03}Ti_{0.28})_{\sum=2.84}(Si_{2.87}Al_{1.13})_{\sum=4.00}O_{10}(OH)_2$
	7	$(K_{0.92}Na_{0.08})_{\sum=1.00}(Mg_{0.93}Fe_{1.64}Mn_{0.03}Ti_{0.27})_{\sum=2.87}(Si_{2.86}Al_{1.14})_{\sum=4.00}O_{10}(OH)_2$
	8	$(K_{0.91}Na_{0.08})_{\sum=1.00}(Mg_{0.91}Fe_{1.64}Mn_{0.03}Ti_{0.27})_{\sum=2.85}(Si_{2.88}Al_{1.12})_{\sum=4.00}O_{10}(OH)_2$
	9	$(K_{0.92}Na_{0.08})_{\sum=1.00}(Mg_{0.94}Fe_{1.63}Mn_{0.03}Ti_{0.27})_{\sum=2.87}(Si_{2.86}Al_{1.14})_{\sum=4.00}O_{10}(OH)_2$
	10	$(K_{0.90}Na_{0.08})_{\sum=0.98}(Mg_{0.95}Fe_{1.69}Mn_{0.04}Ti_{0.26})_{\sum=2.93}(Si_{2.75}Al_{1.25})_{\sum=4.00}O_{10}(OH)_2$
	11	$(K_{0.91}Na_{0.08})_{\sum=1.00}(Mg_{0.91}Fe_{1.64}Mn_{0.03}Ti_{0.27})_{\sum=2.85}(Si_{2.88}Al_{1.12})_{\sum=4.00}O_{10}(OH)_2$
	12	$(K_{0.91}Na_{0.08})_{\sum=0.99}(Mg_{0.93}Fe_{1.71}Mn_{0.03}Ti_{0.27})_{\sum=2.94}(Si_{2.83}Al_{1.17})_{\sum=4.00}O_{10}(OH)_2$
	Avg	$(K_{0.91}Na_{0.08})_{\sum=0.99}(Mg_{0.93}Fe_{1.66}Mn_{0.03}Ti_{0.27})_{\sum=2.89}(Si_{2.84}Al_{1.16})_{\sum=4.00}O_{10}(OH)_2$

of the elemental composition showed that the Fe and K contents of the $4M_2$ Fe-rich biotite were apparently greater than those of the $4A_8$ Fe-rich biotite, whereas the contents of other elements showed only a very small difference between the two polytypes (Table 1, Figs. 5a and S5a,b).

Discussion

The Non-equilibrium Nucleation of the two 4-layer Polytypes

Under the crystallization conditions for a specific geological environment, a specific mineral species will have an identical crystal structure and chemical

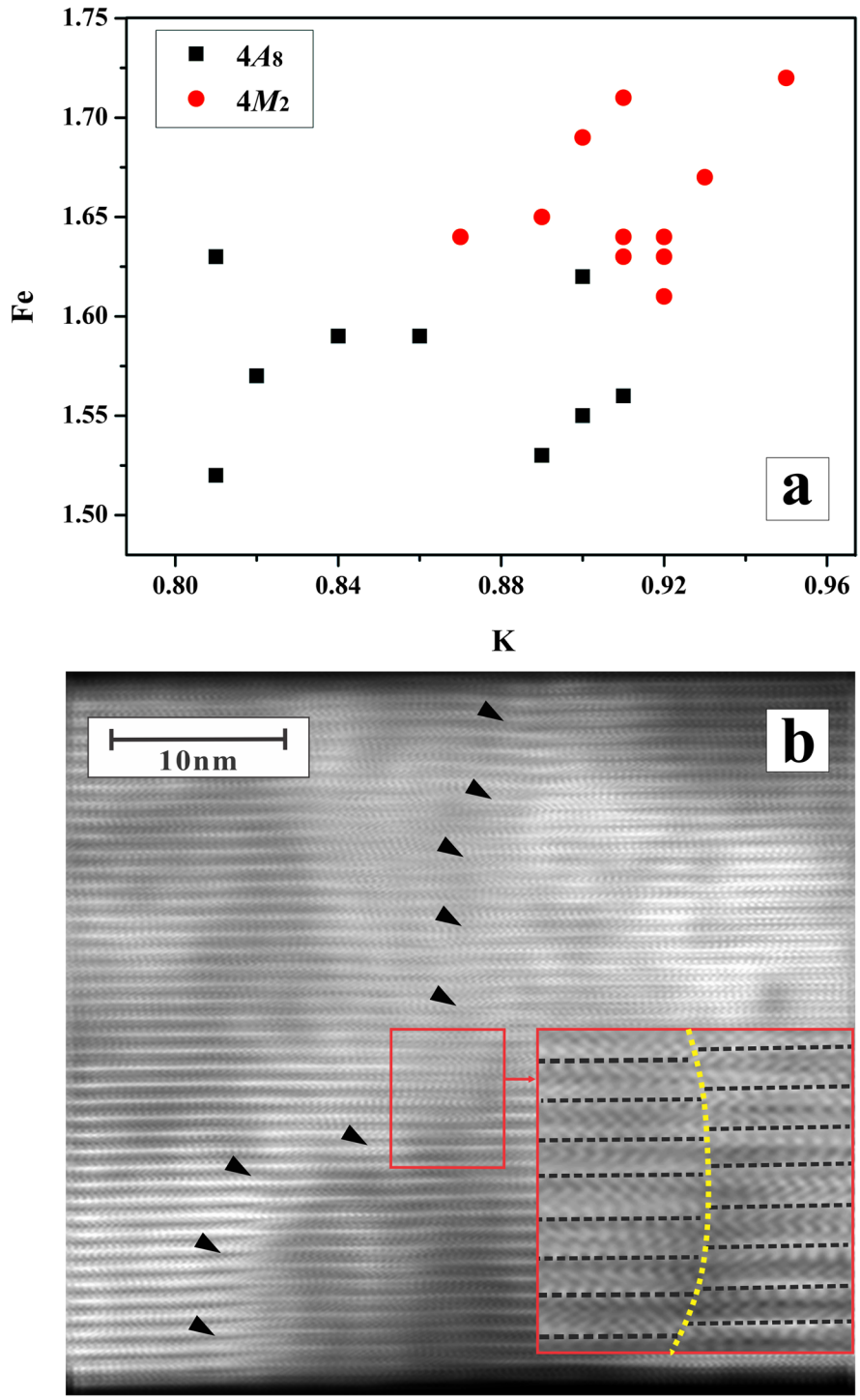

Fig. 5 **a** Diagram showing the relationship between the K and Fe contents of $4M_2$ and $4A_8$ biotite crystals, as calculated using the cation coordination number. **b** HRSTEM image showing screw dislocations (indicated by the black triangles) throughout a $4A_8$ biotite domain. Enlarged red box in **b** shows a screw dislocation with layers on both sides of the dislocation indicated by means of a black dotted line and the dislocation line indicated with a dotted yellow line

composition (Verma & Krishna, 1966). Different mica polytypes, however, may coexist in a specimen (Kogure & Nespolo, 1999; Pignatelli & Nespolo, 2011; Pignatelli et al., 2011; Ross et al., 1966; Rule et al., 1987). Formation of mica polytypes is a two-stage process, and various basic structures form during the early dislocation-free nucleation and growth process (Baronnet & Kang, 1989). The formation of complex polytypes is generally considered to be induced by heterogeneous nucleation (Baronnet, 1992; Penn & Banfield, 1998). The coexistence of multiple short/complex polytypes is considered to be related to complex nucleation under non-equilibrium crystallization conditions (Pignatelli et al., 2016; Xu & Veblen, 1995). This process explains why complex polytypes occur mainly in rocks related to volcanic eruption, mostly rhyolites (Kogure & Nespolo, 1999; Pignatelli et al., 2016; Ross et al., 1966).

During processes involving rapid eruption and cooling, mineral crystallization occurs rapidly; the differences between local composition and crystallization environment of the magma are, therefore, recorded by mineral structures that are sensitive to small compositional variations, such as micas. Consequently, the complexity of the stacking structure can reflect the variations in crystallization environments determined by the oscillations in local microstructure and chemical composition.

From the perspective of structural equivalence, the two 4-layer mica polytypes can be simplified to a combination of standard polytypes: $1M+1M+2M_1$ for $4A_8$ and $1M+3T$ for $4M_2$. The $4A_8$ and $4M_2$ polytypes are probably a result of structure oscillation between different basic polytypes, i.e. $1M$, $2M_1$, and $3T$. Previous studies have suggested that changes in temperature, pressure, and local composition can result in variations in the relative energies of the potential wells for the $1M$, $2M_1$, and $3T$ polytypes (Xu & Veblen, 1995). The $1M$ polytype is the most common form occurring in biotite in nature, followed by $2M_1$, and then $3T$, as the latter two are less stable (Ferraris & Ivaldi, 2002; Nespolo, 2001; Nespolo et al., 1999; Xu & Veblen, 1995). The greater stability of $1M$ has been shown experimentally by monotropic transformations of other polytypes to the unique $1M$ structure for trioctahedral species (Baronnet, 1992; Yoder & Eugster, 1955). Nevertheless, the $2M_1$ and $3T$ polytypes can still form metastably under special conditions. Crystallization processes will be affected by an external force that is induced by compositional fluctuation of an ore-forming fluid, like rapid cooling. The structural oscillation among the $1M$, $2M_1$, and $3T$ polytypes, due to complex interactions between growing crystals and external forces, leads to a non-periodic or even chaotic stacking sequence like that observed in interstratified layer silicates (Wang & Xu, 2006). Such structural oscillations provide the basic structures for subsequent stable periodic repetition of complex polytypes driven by dynamic factors such as screw dislocations.

As mentioned above, the compositional variations provide a dynamic driving force for structural oscillation (Baronnet, 1992; Ross et al., 1966; Smith & Yoder, 1956). According to the EDS results (Table 1, Figs. 5a and S5a,b), the Fe and K contents between the two 4-layer Fe-rich biotite polytypes were different. As is shown in Table 1 and Fig. 5a, the $4A_8$ Fe-rich biotite domains have lower K and Fe contents than the $4M_2$ Fe-rich biotite domains. Baronnet (1992) proposed that the type and number of octahedral and interlayer cations can affect polytype formation considerably. Note that the K and Fe contents of the $4M_2$ polytype Fe-rich biotite were closer to those of $1M$, which is the most stable biotite polytype, and higher than those of the $4A_8$ Fe-rich biotite domains (Table 1 and Fig. S5a). Table 1 shows that the $4A_8$ polytype features more interlayer and octahedral vacancies in its structure, with higher charge density and higher energy, and therefore lower stability than the $4M_2$ and $1M$ polytypes. To some extent, this result can explain the rare occurrence of $4A_8$ in nature relative to $4M_2$ (Ross et al., 1966; Takeda & Donnay, 1965). These complex polytypes formed under rapid cooling from melts, owing to the kinetic barriers preventing the transformation of the polytype phases into the more stable state (i.e. $1M$ polytype of biotite).

The Growth Mechanism of 4-layer Polytypes

Previous studies have proposed that the formation of complex/long-period polytypes may be due to spiral growth via the oriented attachment of several primary mica platelets (He et al., 2021; Penn & Banfield, 1998). Also, the formation of polytypes was attributed to structural control between successive layers during the layer-by-layer growth (Gilmer, 1977; Stranski, 1928). As described above, biotite

commonly occurs in nature as the 1 *M* polytype because of its thermodynamic stability. However, when crystal growth conditions fluctuate, complex polytypes with stacking sequences involving more than one standard structure can be generated. The equilibrium and kinetic theories related to spiral growth have been used to interpret the formation of long-range ordered complex polytypes (Baronnet, 1992; Baronnet & Amouric, 1986; Baronnet et al., 1976; Vand & Hanoka, 1967). Instead of standard biotite polytypes (i.e. 1*M*, $2M_1$, $2M_2$, 2*O*, 3*T*, and 6*H*; the 6*H* polytype has never been found and the 2*O* polytype has been reported only once, by Ferraris et al. in 2001), other mica polytypes are formed by spiral growth in the last differentiation stage of magma (Ramsdell, 1947; Sunagawa et al., 1968; Pignatelli et al., 2011). Complex polytypes can result from screw dislocations generated by the imperfect oriented attachment of several nanoparticles during the early growth stages (Penn & Banfield, 1998). Specifically, if two crystals with different stacking sequence come into contact, one domain can simply grow on the surface of the other by spiral growth, leading to a new stacking sequence. At the contact position, the presence of some transition layers, permitted by the necessary structural adjustment between the two, can be observed (He et al., 2021; Nespolo, 2001) or not (as in this case). Such a growth mechanism leads to a Burgers vector equal to, or an integral multiple of, the repeat distance of the new basic structure (Baronnet, 1992; Baronnet & Amouric, 1986; Fregola et al., 2009; Nespolo, 1999; Vand & Hanoka, 1967).

This growth mechanism can be applied to the formation of the two 4-layer polytypes. The HRSTEM images (Fig. 5b) provide direct evidence of spiral growth, with extensive screw dislocations occurring throughout the $4A_8$ polytype Fe-rich biotite domain (indicated by black triangles in Fig. 5b). Similar screw dislocations are found in all investigated domains of 4-layer Fe-rich biotite. Spiral growth provides a mechanism for a 4-layer nucleus of Fe-rich biotite to produce long-range ordered structures. The mechanism also explains the origin of complex long-period polytypes of micas. Combined with the theory of heterogeneous nucleation and spiral growth theories, the occurrence of ordered complex polytypes generally indicates a fluctuating environment and non-equilibrium conditions of crystallization, during rapid cooling (Pignatelli et al., 2016; Ross et al., 1966).

Summary and Conclusions

Five biotite polytypes (i.e. 1*M*, $2M_1$, 3*T*, $4M_2$, and $4A_8$) were identified in the Fe-rich biotite phenocrysts within rhyolite from the Long Valley Caldera, California. The $4A_8$ polytype is reported in a natural sample for the first time. The structure of the two 4-layer polytypes (i.e. $4M_2$ and $4A_8$) were determined by SAED patterns, 1D lattice images, and HRSTEM images. By using quantitative EDS measurements, a small difference in chemical composition between the two 4-layer polytypes was found, i.e. the $4M_2$ Fe-rich biotite has slightly greater Fe and K contents than $4A_8$ Fe-rich biotite.

The coexistence of these polytypes occurs because of rapid cooling and changes of crystallization environments during volcanic eruption, resulting in chemical and structural oscillations and complex nucleation processes, owing to the decompression and degassing of the melts. Although the most abundant polytype in biotite is 1*M*, other polytypes with high formation energies also occur in the non-equilibrium crystallization environment of the rhyolite magma. Screw dislocations resulting in spiral growth provide a mechanism for the long-range order of these uncommon polytypes. The results from the current investigation suggest an inhomogeneous nucleation and growth mechanism that affects the stacking sequence of biotite. This mechanism explains the origin of long-period polytypes and the intergrowths of diverse polytypes formed during non-equilibrium crystallization.

Funding This study was supported financially by the National Natural Science Foundation of China (Grant Nos. 41921003, 41825003, and 42072044), Youth Innovation Promotion Association CAS (Grant No. 2018387), the Department of Science and Technology of Guangdong Province (Grant No. 2017GC010128 and 2019TX05L169), and the Science and Technology Planning of Guangdong Province, China (2020B1212060055).

Declarations

Conflict of Interest The authors declare that they have no conflict of interest.

References

Bailey, S. W. (1984). Review of cation ordering in micas. *Clays and Clay Minerals, 32*, 81–92.

Banfield, J. F., & Murakami, T. (1998). Atomic-resolution electron microscope evidence for the mechanism by which chlorite weathers to 1:1 semi-regular chlorite-vermiculite. *American Mineralogist, 83*, 348–357.

Baronnet, A. (1992). Polytypism and stacking disorder. *Minerals and Reactions at the Atomic Scale, 27*, 231–288.

Baronnet, A., & Amouric, M. (1986). Growth spirals and complex polytypism in micas. II. occurrence frequencies in synthetic species. *Bulletin de Mineralogie, 109*, 489–508.

Baronnet, A., & Kang, Z. C. (1989). About the origin of mica polytypes. *Phase Transitions, 16*, 477–493.

Baronnet, A., Amouric, M., & Chabot, B. (1976). Mécanismes de croissance, polytypisme et polymorphisme de la muscovite hydroxylée synthétique. *Journal of Crystal Growth, 32*, 37–59.

Baronnet, A., Nitsche, S., & Kang, Z. C. (1993). Layer stacking microstructures in a biotite single crystal: A combined HRTEM–AEM study. *Phase Transitions, 143*, 107–128.

Bigi, S., & Brigatti, M. F. (1994). Crystal chemistry and microstructures of plutonic biotite. *American Mineralogist, 79*, 63–72.

Bozhilov, K. N., Xu, Z., Dobrzhinetskaya, L. F., Jin, Z. M., & Green, H. W. (2009). Cation-deficient phlogopitic mica exsolution in diopside from garnet peridotite in SuLu, China. *Lithos, 109*, 304–313.

Brigatti, M. F., & Guggenheim, S. (2002). Mica crystal chemistry and the influence of pressure, temperature, and solid solution on atomistic models. *Reviews in Mineralogy and Geochemistry, 46*, 1–97.

Brigatti, M. F., Guidotti, C. V., Malferrari, D., & Sassi, F. P. (2008). Single-crystal X-ray studies of trioctahedral micas coexisting with dioctahedral micas in metamorphic sequences from western Maine. *American Mineralogist, 93*, 396–408.

Ferraris, G., & Ivaldi, G. (2002). Structural features of micas. *Reviews in Mineralogy and Geochemistry, 46*, 117–153.

Ferraris, G., Gula, A., Ivaldi, G., Nespolo, M., Sokolova, E., Uvarova, Y., & Khomyakov, P. (2001). First structure determination of an MDO-2*O* mica polytype associated with a 1*M* polytype. *European Journal of Mineralogy, 13*, 1013–1023.

Fregola, R. A., & Scandale, E. (2011). A 94-layer long-period mica polytype: A TEM study. *American Mineralogist, 96*, 172–178.

Fregola, R. A., Capitani, G., Scandale, E., & Ottolini, L. (2009). Chemical control of 3*T* stacking order in a Li-poor biotite mica. *American Mineralogist, 94*, 334–344.

Gilmer, G. H. (1977). Computer simulation of crystal growth. *Journal of Crystal Growth, 42*, 3–10.

Guggenheim, S., Bain, D. C., Bergaya, F., Brigatti, M. F., Drits, V. A., Eberl, D. D., Formoso, M. L., Galán, E., Merriman, R. J., Peacor, D. R., Stanjek, H., & Watanabe, T. (2002). Report of the association internationale pour l'étude des argiles (AIPEA) nomenclature committee for 2001: Order, disorder and crystallinity in phyllosilicates and the use of the "crystallinity index." *Clays and Clay Minerals, 50*, 406–409.

Guinier, A., Bokij, G. B., Boll-Dornberger, K., Cowley, J. M., Jagodzinski, H., Krishna, P., Zvyagin, B. B., Cox, D. E., Goodman, P., Hahn, Th., Kuchitsu, K., & Abrahams, S. C. (1984). Nomenclature of polytype structures. Report of the International Union of Crystallography Ad-Hoc Committee on the Nomenclature of Disordered, Modulated, and Polytype Structures. *Acta Crystallographica, A40*, 399–404.

Güven, N, & Burnham, C. W. (1967). The crystal structure of 3*T* muscovite. *Zeitschrift Für Kristallographie Crystalline Materials, 125*, 163–183.

He, H. P., Yang, Y. P., Ma, L. Y., Su, X. L., Xian, H. Y., Zhu, J. X., Teng, H., & Guggenheim, S. (2021). Evidence for a two-stage particle attachment mechanism for phyllosilicate crystallization in geological processes. *American Mineralogist, 106*, 983–993.

Hooper, W. P., & Eloranta, E. W. (1986). Lidar measurements of wind in the planetary boundary layer: The method, accuracy and results from joint measure-ments with radiosonde and kytoon. *Journal of Climate and Applied Meteorology, 25*, 990–1001.

Iijima, S., & Buseck, P. R. (1978). Experimental study of disordered mica structures by high-resolution electron microscopy. *Acta Crystallographica, A34*, 709–719.

Kogure, T. (2002). Investigations of micas using advanced transmission electron microscopy. *Reviews in Mineralogy and Geochemistry, 46*, 281–312.

Kogure, T., & Banfield, J. F. (1998). Direct identification of the six polytypes of chlorite characterized by semi-random stacking. *American Mineralogist, 83*, 925–930.

Kogure, T., & Nespolo, M. (1999). TEM study of long-period mica polytypes: Determination of the stacking sequence of oxybiotite by means of atomic resolution images and Periodic Intensity Distribution (PID). *Acta Crystallographica Section B - Structural Science, 55*, 507–516.

Lacalamita, M., Mesto, E., Scordari, F., & Schingaro, E. (2012a). Chemical and structural study of 1*M*- and $2M_1$ - phlogopites coexisting in the same Kasenyi kamafugitic rock (SW Uganda). *Physics and Chemistry of Minerals, 39*, 601–611.

Lacalamita, M., Scordari, F., Schingaro, E., & Mesto, E. (2012b). Crystal chemistry of trioctahedral micas - $2M_1$ from Bunyaruguru (SW Uganda) kamafugite. *American Mineralogist, 97*, 430–439.

Laurora, A., Brigatti, M. F., Mottana, A., Malferrari, D., & Caprilli, E. (2007). Crystal chemistry of trioctahedral micas in alkaline and subalkaline volcanic rocks: A case study from Mt. Sassetto (Tolfa district, Latium, central Italy). *American Mineralogist, 92*, 468–480.

Metz, J. M., & Mahood, G. A. (1991). Development of the long valley, California, magma chamber recorded in precaldera rhyolite lavas of glass mountain. *Contributions to Mineralogy and Petrology, 106*, 379–397.

Nespolo, M. (1999). Analysis of family reflections of OD mica polytypes, and its application to twin identification. *Mineralogical Journal, 21*, 53–85.

Nespolo, M. (2001). Perturbative theory of mica polytypism. Role of the M2 layer in the formation of inhomogeneous polytypes. *Clays and Clay Minerals, 49*, 1–23.

Nespolo, M., & Ďurovič, S. (2002). Crystallographic basis of polytypism and twinning in micas. In A. Mottana, F. P. Sassi, & J. B. S. ThompsonGuggenheim (Eds.), *Micas: Crystal chemistry and metamorphic petrology* (pp. 155–279). Springer.

Nespolo, M., Takeda, H., Kogure, T., & Ferraris, G. (1999). Periodic intensity distribution (PID) of mica polytypes: Symbolism, structural model orientation and axial settings. *Acta Crystallographica Section A, 55*, 659–676.

Pauling, L. (1930). The rotational motion of molecules in crystals. *Physical Review, 36*, 430–443.

Penn, R. L., & Banfield, J. F. (1998). Oriented attachment and growth, twinning, polytypism, and formation of metastable phases: Insights from nanocrystalline TiO_2. *American Mineralogist, 83*, 1077–1082.

Pennycook, S. J. (2002). Structure determination through Z-contrast microscopy. *Advances in Imaging & Electron Physics, 123*, 173–206.

Pignatelli, I., & Nespolo, M. (2011). $5M_3$ ferriphlogopite from the Ruiz Peak (New Mexico, USA): First occurrence of a mica polytype with coexistence of M1- and M2- layers. *European Journal of Mineralogy, 23*, 703–715.

Pignatelli, I., Dusek, M., De Titta, G., & Nespolo, M. (2011). Structural modelling, refinement and possible formation mechanism of a $4M_3$ non-MDO ferriphlogopite (Ruiz Peak volcano). *European Journal of Mineralogy, 23*, 73–84.

Pignatelli, I., Faure, F., & Mosser-Ruck, R. (2016). Self-mixing magma in the Ruiz Peak rhyodacite (New Mexico, USA): A mechanism explaining the formation of long period polytypes of mica. *Lithos, 266*, 332–347.

Ramsdell, L. S. (1947). Studies on silicon carbide. *American Mineralogist, 32*, 64–82.

Ross, M., Takeda, H., & Wones, D. R. (1966). Mica polytypes: Systematic description and identification. *Science, 151*, 191–193.

Rule, A. C., Bailey, S. W., Livi, K. J., & Veblen, D. R. (1987). Complex stacking sequence in a lepidotite from Tørdal, Norway. *American Mineralogist, 72*, 1163–1169.

Smith, J. V., & Yoder, H. S. (1956). Experimental and theoretical studies of the mica polymorphs. *Mineralogical Magazine, 31*, 209–235.

Stöckhert, B. (1985). Compositional control on the polymorphism $2M_1$ - $3T$ of phengitic white mica from high pressure parageneses of the Sesia Zone (lower Aosta valley, Western Alps; Italy). *Contributions to Mineralogy and Petrology, 89*, 52–58.

Stranski, I. N. (1928). Zur Theorie des Kristallwachstums. *Zeitschrift Für Physikalische Chemie, 136*, 259–278.

Sunagawa, I., Endo, Y., Daimon, N., & Tate, I. (1968). Nucleation, growth and polytypism of flour-phlogopite from the vapour phase. *Journal of Crystal Growth, 3*, 751–751.

Takeda, H., & Donnay, J. (1965). A standardized Japanese nomenclature for crystal forms. *Mineralogical Journal, 4*, 291–298.

Takeda, H., & Ross, M. (1975). Mica polytypism - dissimilarities in crystal-structure of coexisting $1M$ and $2M_1$ biotite. *American Mineralogist, 60*, 1030–1040.

Takeda, H., & Ross, M. (1995). Mica polytypism: Identification and origin. *American Mineralogist, 80*, 715–724.

Tomisaka, T. (1958). On the chemical properties, optical properties and the structural types of some muscovites and phlogopites. *Journal of the Mineralogical Society of Japan, 3*, 710–721.

Tomisaka, T. (1962). Polytypes of the phlogopite-biotite series and their mutual relations. *Journal of Mineralogy Petrology and Economic Geology, 47*, 134–143.

Vand, V., & Hanoka, J. I. (1967). Epitaxial theory of polytypism; observations on the growth of PbI_2 crystals. *Materials Research Bulletin, 2*, 241–251.

Verma, A. R., & Krishna, P. (1966). Crystallography: Exploring Polytypism. (Book reviews: polymorphism and polytypism in crystals). *Science, 154*, 1316.

Wang, Y. F., & Xu, H. F. (2006). Geochemical chaos: Periodic and nonperiodic growth of mixed-layer phyllosilicates. *Geochimica Et Cosmochimica Acta, 70*, 1995–2005.

Xu, H. F., & Veblen, D. R. (1995). Periodic and nonperiodic stacking in biotite from the Bingham Canyon porphyry copper deposit, Utah. *Clays and Clay Minerals, 43*, 159–173.

Xu, H. F., Shen, Z., Konishi, H., & Luo, G. (2014). Crystal structure of Guinier-Preston zones in orthopyroxene: Z-contrast imaging and ab inito study. *American Mineralogist, 99*, 2043–2048.

Xu, H. F., Shen, Z., & Konishi, H. (2015). Natural occurrence of monoclinic Fe_3S_4 nano-precipitates in pyrrhotite from the Sudbury ore deposit: A Z-contrast imaging and density functional theory study. *Mineralogical Magazine, 79*, 377–385.

Yoder, H. S., & Eugster, H. P. (1955). Synthetic and natural muscovites. *Geochimica Et Cosmochimica Acta, 8*, 225–284.

Zhukhlistov, A. P., Zvyagin, B. B., & Pavlishin, V. L. (1988). Biotite $4M$ with an inhomogeneous layer alternation. *Zeitschrift fur Kristallographie, 185,* 624.

Zvyagin, B. B. (1987). Polytypism in contemporary crystallography. *Soviet Physics Crystallography, 32*, 394–399.

Zvyagin, B. B. (1997). Modular analysis of crystal structures. *EMU Notes in Mineralogy, 1*, 345–372.